



Co-sputtering of lithium vanadium oxide thin films with variable lithium content to enable advanced solid-state batteries

Journal:	<i>Journal of Materials Chemistry A</i>
Manuscript ID	TA-ART-02-2022-001021.R2
Article Type:	Paper
Date Submitted by the Author:	16-May-2022
Complete List of Authors:	<p>Castagna Ferrari, Victoria; University of Maryland at College Park, Materials Science and Engineering; University of Maryland at College Park Institute for Research in Electronics and Applied Physics,</p> <p>Soo Kim, Nam; University of Maryland at College Park, Chemistry and Biochemistry</p> <p>Lee, Sang Bok; University of Maryland at College Park, Chemistry and Biochemistry</p> <p>Rubloff, Gary; University of Maryland at College Park, Materials Science and Engineering; University of Maryland at College Park Institute for Research in Electronics and Applied Physics, ; University of Maryland Institute for Systems Research</p> <p>Stewart, David; University of Maryland at College Park, Materials Science and Engineering; University of Maryland at College Park Institute for Research in Electronics and Applied Physics,</p>

ARTICLE

Co-sputtering of lithium vanadium oxide thin films with variable lithium content to enable advanced solid-state batteries

Victoria C. Ferrari,^{ab} Nam S. Kim^c, Sang Bok Lee^c, Gary W. Rubloff^{abd} and David M Stewart^{*ab}

Received 00th January 20xx,
Accepted 00th January 20xx

DOI: 10.1039/x0xx00000x

Advanced solid-state batteries most likely will entail aggressive structures or architectures with constraints that typically limit processing temperatures. Considering this, we have identified the importance of providing lithiated electrode material at a modest processing temperature. Here we describe a pathway to meet this by the development of a co-sputtering process using lithium oxide and vanadium oxide targets which enables the growth of lithiated vanadium oxide (LVO) thin films for application in solid-state batteries. Analysis of the structure and film composition of samples deposited with different co-sputtering rate ratios and post-annealing shows that multiple phases of $\text{Li}_x\text{V}_2\text{O}_5$ likely coexist (i.e. α -, ϵ -, δ -, and γ - V_2O_5), and that this is unchanged after electrochemical cycling. The co-sputtering process can tune the lithium content up to a highly lithiated state of at least $\text{Li}_2\text{V}_2\text{O}_5$. Electrochemical half-cells showed a significant amount of lithium available on the first charge (delithiation of LVO). LVO samples post-annealed at 300 °C showed typical redox peaks for $\text{Li}_x\text{V}_2\text{O}_5$ for both one and two lithium insertion reactions, which were highly reversible in most cases. A thin-film solid-state battery prototype using LVO as a cathode had 20 % of the expected capacity, although the coulombic efficiency is near 100 % at a fast rate (22C). This co-sputtering technique represents an opportunity for low temperature synthesis of pre-lithiated cathodes for thin film batteries, and introduces a broader methodology of depositing metal oxides with different alkali metal contents.

Introduction

Lithium-ion batteries (LIBs) enabled a technological revolution in portable devices, hybrid and electric vehicles, and smart devices. However, the majority of commercially available LIBs employ flammable liquid electrolytes, which increase the risk of excessive heating and possible internal short circuits.^{1,2} For this reason and more, solid-state batteries (SSBs) are anticipated as the next energy storage technology to replace present-day LIBs.³ For certain applications in biomedical devices and electronics, thin-film SSBs are an important architecture, compatible with many well-established micro-fabrication processes for electronics integration. Borrowing techniques from the micro-electronics industry, important factors regarding scalability, processing cost, and flexibility in shape and size are generally applicable to thin-film SSBs.^{4–6}

A step toward more advanced SSB structures is depicted in Figure 1, for which we have developed a thin film fabrication strategy and modelled its performance and scaling. The

structure demonstrates the importance of incorporating Li into either anode or cathode materials directly during their deposition and serves as an example of the processing requirements for thin-film-fabricated solid-state batteries. To maximize energy and power density, thin electrode-electrolyte-electrode layers should be configured to maximize the surface area, and so the interfaces become the dominant part of the system. Thin film fabrication should avoid thermal stress which causes mechanical failure, unwanted surface contamination which inhibits the electrochemical reactions, and any processing steps which expose the most reactive layers (typically the electrolyte or anode) to oxygen or moisture.

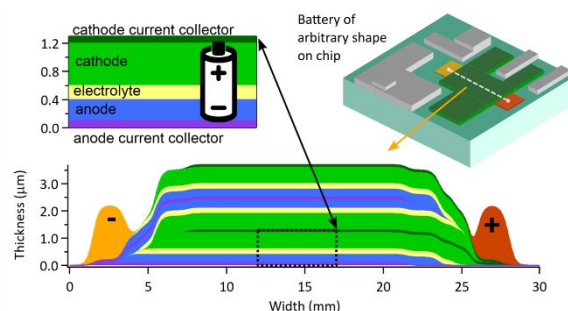


Figure 1: Cross section of a representation of an advanced solid-state battery, which leverages thin film processing to stack multiple layers of anode, electrolyte, and cathode in a manner which magnifies the energy storage for a given device footprint. Such batteries may be made in arbitrary shapes and intimately integrated into micro-electronics devices. The total number of battery layers depicted is small, but would scale depending on the desired performance.

^a Department of Materials Science and Engineering, University of Maryland, College Park, Maryland 20742, United States

^b Institute for Research in Electronics and Applied Physics, University of Maryland, College Park, Maryland 20742, United States

^c Department of Chemistry and Biochemistry, University of Maryland, College Park, Maryland 20742, United States

^d Institute for Systems Research, University of Maryland, College Park, Maryland 20742, United States

Electronic Supplementary Information (ESI) available: [Additional XPS data of V_2O_5 and C 1s and Li 1s from LVO samples; electrochemistry data for sputtered V_2O_5 post-annealed at 500 °C; additional electrochemical data for LVO 90W T25 and T300 samples; top-view SEM images of LVO samples]. See DOI: 10.1039/x0xx00000x

Among the benefits of using thin-film SSBs, the well-defined surface area obtained from physical vapor deposition (PVD) techniques allows excellent characterization of electrochemical and electrical properties for further development of individual constituent layers.^{5,7} More practically, the diffusion lengths needed for electrons and lithium ions are smaller in thinner films, which increases the power density of SSBs and reduces internal resistances.^{2,8–11} High energy density is also desirable, and it can be maximized by the choice of electrode material couples and by stacking multiple thin film SSB layers as depicted in Figure 1.

Each electrode material will have electrochemical phase transformations occur at different voltages. Both the capacity and voltage of the electrochemical reactions is relevant to the performance of the device, where a larger voltage difference between the anode and cathode reactions results in larger energy density. Layered oxides are generally good cathode candidates, with lithium cobalt oxide (LCO) being the most commonly used in commercial portable electronics due to its high capacity and high voltage where electrochemical reactions of lithium insertion/extraction occur.¹² Typically it is necessary to anneal sputter deposited lithium cobalt oxide (LCO) at 500 °C to achieve the correct phase. While good electrochemical activity has been reported for electrodeposited LCO at only 260 °C^{6,13}, switching between vacuum and liquid processes for each battery layer render advanced SSB structures like that in Figure 1 much more difficult.

The toxicity and politically fraught sources of cobalt urge the need to find another alternative to LCO cathodes in lithium batteries. The layered oxide vanadium pentoxide (V_2O_5) has been well studied and makes a suitable replacement for lithium cobalt oxide as a cathode material; in fact, Panasonic first used it in commercial batteries as early as the 2000s.¹⁴ The intercalation of one lithium ion per V_2O_5 site corresponds to a theoretical specific capacity of 147 mAh/g of V_2O_5 , which is comparable to lithium cobalt oxide's capacity. However, the voltage of the Li intercalation of V_2O_5 is relatively lower than LCO. This can be mitigated by the fact that more than one Li can be reversibly intercalated into the V_2O_5 structure with a higher capacity.^{15,16} The insertion of two lithium ions enables a theoretical capacity of 294 mAh/g of V_2O_5 in the voltage range of 2.0 – 4.0 V vs Li/Li+.^{14–22} In traditional LIBs, what limits the use of lithium vanadium oxide (LVO) as a cathode is the slow lithium ion diffusion (10^{-12} – 10^{-13} cm²/s) and poor electrical conductivity (10^{-7} – 10^{-6} S/cm) of V_2O_5 ,^{18,19} but the sluggish transport can be mitigated by making the LVO thin, below a few μ m. Therefore, in the context of thin film SSBs, the challenge is producing LVO thin films with controlled Li content in a process compatible with the deposition of subsequent electrolyte and electrode layers.

Several works successfully produced crystalline and amorphous vanadium oxide thin films using rf-magnetron sputtering from a V_2O_5 target and reacting with an argon and oxygen atmosphere.^{23–26} Since pure V_2O_5 is produced, this process is primarily used for batteries with lithium containing anodes. For a lithium free anode, the V_2O_5 is typically lithiated electrochemically post-deposition by immersion in liquid

electrolyte, a process which is impractical for thin film fabrication at scale, particularly for advanced architectures such as depicted in Figure 1. One way to avoid electrochemical lithiation is depositing lithiated vanadium oxide by co-sputtering with a Li source.

Co-sputtering and multilayered sputter deposition have been implemented as good methodologies to increase the amount of lithium in thin-film anodes, like $Li_4Ti_5O_{12}$ (LTO), and in solid electrolytes such as lithium garnets ($Li_7La_3Zr_2O_{12}$). A lithium oxide target was proven to effectively serve as a supplementary lithium source for those thin-films which usually showed a loss of lithium after sputter deposition due to high-temperature annealing, while in this work it is the primary source of lithium.^{27–30} One prior report studied the synthesis of LVO using a vanadium oxide target and lithium phosphate target (Li_3PO_4) as V_2O_5 and Li sources, respectively³¹. They did not present variations of co-sputtering conditions to fabricate cathode materials with different amounts of lithium, and the product of their co-sputtering process showed an electrochemically active cathode material, but with a modest charge/discharge capacity and a loss of 49 % between the first and the 30th discharge cycles.

Herein, our study reports a promising LVO cathode for thin film SSBs made by co-sputtering of V_2O_5 and lithium oxide (Li_2O). In this case the Li_2O is the primary and only source of lithium during deposition. The thin films showed an electrochemical capacity up to 114 and 222 mAh/g in one lithium and two lithium insertion windows, respectively, when post-annealed at 300 °C, during liquid cell testing. The co-sputtering process could, therefore, pre-lithiate the vanadium oxide during deposition in a high-vacuum process that produced electrochemically active films. As a proof-of-concept, solid-state batteries were fabricated using co-sputtered LVO and a lithium-free anode (silicon) to confirm that the lithium ions could be cycled in a solid-state device. The capacity is about 20 % of the expected value for one-lithium insertion, but the devices worked even at very high C-rates (22C). More optimizations can be done on those SSBs for future applications in microelectronics. Furthermore, the investigation discussed here can provide an avenue to fabricate cathode materials with different ions, such as sodium and magnesium, and expand opportunities for SSB design and fabrication.

Methodology

LVO samples were fabricated using a co-sputtering process, by striking both 2-inch diameter V_2O_5 and Li_2O targets at the same time inside a UHV chamber. In this case, the substrate was a Si wafer that was previously coated with 500 nm of SiO_2 , a 10 nm Ti adhesion layer, and finally a 50 nm Au thin film, which served as the current collector for electrochemical measurements. Co-sputter depositions were done in an AJA ATC Orion 8 Sputter tool, with a 13 cm target-to-substrate distance. Both targets' power was ramped up/down in 900 s in 30 sccm of argon at 25 mTorr of pressure. For deposition the pressure was reduced to 1.5 mTorr, established using 12 sccm of argon for co-sputtered processes and 11 sccm of argon with 1 sccm of

oxygen for pure V_2O_5 deposition. A common deposition time of 3 hours was used for all films.

To investigate the deposition parameters, four different LVO films were produced using two different variables: the power of the Li_2O target, and a post-annealing step. Different levels of Li_2O target power were tested, but no significant amount of lithium could be extracted during electrochemical testing when the target power was below 60 W. For the annealing, the substrate was heated to 300 °C before leaving the sputtering chamber, i.e., in-situ, and held there for three hours. During this time the chamber was held at 1.5 mTorr using 25 sccm of nitrogen gas at 5 mTorr. The following table specifies the notation used for each sample according to these variables.

Table 1: Notation for samples according to the amount of inserted lithium and the heat treatment.

	V_2O_5 target power (W)	Li_2O target power (W)	Heat treatment
LVO 90W T25	153	90	Not used (25 °C)
LVO 90W T300	153	90	Post-anneal 300 °C
LVO 120W T25	153	120	Not used (25 °C)
LVO 120W T300	153	120	Post-anneal 300 °C
V_2O_5	153	0	Deposition at 300 °C

A thin-film solid-state battery (SSB) prototype was fabricated using the same sputter tool, with a sequence of shadow masks exchanged in situ, for all of the components of the battery, with no exposure to atmosphere between layers. On a 3-inch silicon wafer with 500 nm thermal SiO_2 layer, the multilayer sputter deposition started with a Ti/Au layer as a cathode current collector. Using a shadow mask to delineate the cathode and electrolyte areas, LVO 120W T300 film was deposited, followed by a LiPON deposition at 65 W and 1.5 mTorr. Another shadow mask was used to deposit 90 nm of amorphous silicon at 90 W and 5 mTorr to be the anode and 100 nm of copper at 280 W and 3 mTorr was deposit to be the anode current collector. After all of these deposition steps, a post-annealing was done on the whole stack using the same conditions described for the LVO process development. The shadow masks were changed inside a low-vacuum pre-chamber connected to the sputter tool, i.e., there was no air exposure at any time during the deposition. 49 devices were patterned successfully with confirmed reproducibility of electrochemical measurements.

For the LVO samples, electrochemical analysis was performed using a beaker cell to check whether the samples were electrochemically active in both the one and two lithium voltage windows (from 2.6 to 4.0 V for one lithium and from 2.0 to 4.0 V for two lithium vs Li^+/Li , respectively). Thereafter, cyclic voltammetry (CV) and galvanostatic charge/discharge cycling tests were done for the first three cycles of charging/discharging to evaluate the capacity retention and reversibility of the different LVO samples. The tests were done using a two-electrode configuration in a beaker cell where both counter electrode and reference electrode were an immersed lithium foil from Alfa Aesar (99.9 %). The electrolyte was 150 mL

of $LiClO_4$ in PC at 1 M concentration. These studies were performed inside an argon glovebox connected to a BioLogic potentiostat. For the SSB prototype, all the testing was done in a potentiostat connected to a probe station inside an argon glovebox with a two-electrode setup. The silicon was connected as the counter-electrode and the reference, while the LVO was the working electrode. For CV measurements, the device was cycled between +1.5 V and -0.2 V. The open-circuit voltage (OCV) was measured as -80 mV. For galvanostatic charge/discharge cycling tests, a current density of 62.4 $\mu A/cm^2$ (which corresponds to about 22C) was applied for 100 cycles.

For a qualitative analysis of their structure, a H-J-Y Raman Microscope was used with a 633 nm laser source having a measured power of 2.1 mW in Raman mode. For every measurement, three 20 s acquisitions were averaged. XRD was also done to analyze their crystallography, but no peaks were located. SEM images in Figure S7 showed the film surfaces to be uniform and homogeneous, though the unannealed films exhibited a nanogranular structure that appears to have been smoothed out by annealing. For characterization of surface composition, a Kratos Axis Ultra DLD XPS system was used with an aluminum monochromatic source. The quantification of the surface composition was done using a high-resolution pass energy of 20 eV and applying a Shirley background. All XPS spectra were charge corrected with respect to the C 1s peak at 284.5 eV. For the depth profile analysis, a 5 kV Ar ion beam was used with a Wien mass filter to repeatedly etch a region 2x2 mm². For the thickness measurements, a J.A. Woollam M-2000D Spectroscopic Ellipsometer was used, and cross-sections were made in a Tescan GAIA FIB/SEM for further confirmation of the obtained values. Energy-Dispersive X-Ray Spectroscopy (EDS) was operated at 20 kV and it was used to analyze elemental composition of the SSBs.

Results and Discussion

Raman spectroscopy. It is commonly used in vanadium oxide systems due its ability to detect structural variations that correspond to lattice distortions during lithiation.³² $Li_xV_2O_5$ exhibits reversible phase transitions as the lattice is distorted. The α -phase occurs at the initial Li-ion intercalation ($x < 0.01$), where the V_2O_5 structure is preserved. The ϵ -phase ($0.35 < x < 0.7$), δ -phase ($0.9 < x < 1$) and γ -phase ($1 < x < 2$) are LVO varieties with increasing lattice distortion, in which the reversibility of insertion/de-insertion of Li-ions from δ -phase to γ -phase may not be completely maintained.^{33,34} Characteristic vibrational modes of V_2O_5 are in a frequency range of 100 to 1100 cm^{-1} .

Figure 2 presents Raman spectra of a crystalline V_2O_5 thin film and the LVO films as-deposited, i.e., with no electrochemical lithiation/delithiation. For the crystalline V_2O_5 sample (Figure 2, spectrum a), a total of 10 vibrational modes were found in this frequency range that are in accordance with previous reports in the literature.^{32,35,36} The vibrations located in the region between 520 and 1000 cm^{-1} correspond to V-O bond stretching modes. In this region, there are only 2 vibrations with well-defined peaks at 700 cm^{-1} and at 996 cm^{-1}

that correspond to the stretching mode of the doubly coordinated oxygen shared at the corners of VO₅ square pyramids, and the apical V-O bond, respectively. The weak peak at 530 cm⁻¹ corresponds to the triply coordinated oxygen shared at the edges of the square pyramid.

In the intermediate frequency region, between 200 and 500 cm⁻¹, there are four peaks related to the bending vibrational modes of the V-O bonds from the layers. Also, three peaks can be identified at 114, 145 and 193 cm⁻¹ which correspond to phonons of each V-O layer, i.e., lattice vibrations that do not correspond to the interaction between different layers.^{35,37} This spectrum suggests that there was a formation of only α -V₂O₅ with no other polymorphs. Some Raman peaks from VO₂ or V₆O₁₃ would be observed if there was an oxygen deficiency^{38,39}; however, their characteristic peaks were not seen for crystalline V₂O₅ thin film in this work.

The lithiated thin films showed different vibrational modes across the spectrum. All the spectra here were acquired using the same parameters to make clear conclusions, and an extended laser beam exposure (360 times longer than was used in Figure 2) did not alter the Raman spectra as it was observed in other references in the literature.^{40,41} Because the signal/noise ratio observed in Raman spectroscopy depends on the acquisition parameters like laser power and acquisition time for lithiated V₂O₅ samples, it is hard to find Raman spectra that perfectly match the vibrational peaks and their sharpness. We were able to match a powdered δ -V₂O₅ phase with the spectrum of LVO 120W T25 sample (Figure 2d) for all the peaks above 200 cm⁻¹,⁴⁰ which is a good indication that we have indeed produced a lithiated vanadium oxide layer from the co-sputtering method. The spectra shown in b and c are from samples deposited at the same Li₂O power, but they clearly have different vibrations due to the annealing process. There are some peaks located in the same frequency range observed for crystalline V₂O₅ thin film such as the peaks between 450 and 550 cm⁻¹ and the peak centered at 725 cm⁻¹, which shows a peak shift and broadening to higher wavenumber when the lithium content is increased.^{32,42,43}

On the other hand, significant changes are observed in the high and low frequency ranges. The as-deposited LVO 90W T25 sample had no post-annealing step, and it showed more Raman peaks than LVO 90W T300 (c.f. spectra b and c). More Raman peaks correspond to more vibrational modes, which can indicate a higher degree of lattice distortion in the sample with no heat treatment. The same behavior can be seen for the two LVO 120W samples (spectra d and e).

The peak close to 1000 cm⁻¹ is directly related to vibrations in the interlayer spacing when lithium is inserted.^{35,37} The lithiated films presented a significant increase in the intensity of this peak with respect to the V₂O₅ spectrum, along with a considerable shift to lower frequencies. Also, there are multiple peaks in the region between 900 and 1000 cm⁻¹ for all LVO samples in comparison to the single peak from V₂O₅. It seems that there are more peaks at higher wavenumbers for the unannealed samples, which could indicate a random and diverse degree of lattice distortion due to Li atoms sitting at different sites.

For the LVO 90W T25 sample (Figure 2b), the peak in this region with the highest intensity is at 984 cm⁻¹, while for LVO 120W T25 (Figure 2d), the most intense peak is at 944 cm⁻¹. Since this region is directly related to the lattice distortion by lithium insertion,⁴⁴ the difference in peak intensity and peak position could be related to the location of the inserted lithium ions, the amount of them in the structure and, therefore, the different lithiated phases of V₂O₅. The α , ϵ , δ and γ phases have their characteristic peaks in this region at 995, 982, 967 and 957 cm⁻¹, respectively.⁴³ Therefore, for all the fabricated LVO samples there are peaks corresponding to more than one phase. Since the LVO 120W T25 sample should have more lithium than the LVO 90W T25 film, it is expected that the lithium ions would occupy more locations. Also, there is one peak at 875 cm⁻¹ for the unannealed samples (LVO 90W T25 and LVO 120W T25, Figures 2b and d, respectively) that could indicate the presence of V₆O₁₃.³⁸ The peak at 700 cm⁻¹ shifted to higher wavenumbers for all the studied LVO samples, but it shifted more for the post-annealed LVO films, which support the hypothesis that the lithium ions are in more thermodynamically stable locations in the post-annealed samples, causing the V-O bonds to be shorter. On the other hand, the peak corresponding to lattice vibrations around 145 cm⁻¹ only appeared in the unannealed samples (LVO 90W T25 and LVO 120W T25) as a small peak.

Therefore, three qualitative conclusions can be made from this set of spectra: i) one contribution to the lattice disorder comes from the lithium insertion; ii) although the post-anneal step somewhat recovers the ordering of the layers (because of the reduction of overall peaks), the improvement is not large; and iii) these observations of the LVO systems show that there may be a non-uniform lithium distribution in the LVO films, having ϵ -V₂O₅, δ -V₂O₅ and γ -V₂O₅ phases coexisting.

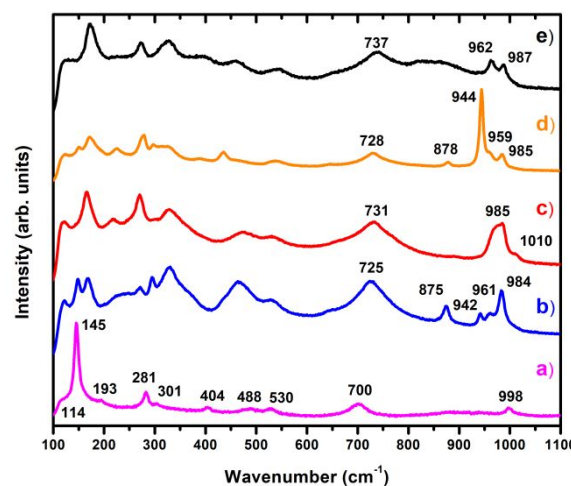


Figure 2: Raman spectra of as-deposited a) crystalline V₂O₅ thin film; b) LVO 90W T25; c) LVO 90W T300; d) LVO 120W T25; and e) LVO 120W T300. These measurements were taken before any electrochemical analysis.

X-Ray Photoelectron Spectroscopy (XPS). It was used to analyze the surface composition of the LVO films after deposition. The samples were exposed to atmosphere when

transferring them from the sputter tool to the XPS equipment, so carbon contamination on the surface was expected. Overall, all the studied films presented a small amount of carbon at the surface (less than 8 at %) except the LVO 90W T300 film, which showed 17 at % of carbon. This is the first indication that the surface of this specific sample is more reactive than the other LVO films. C 1s and Li 1s spectra were taken for the LVO samples to determine the full surface composition of the films. From the results of C 1s spectra (see Table 2 and Figure S2a), all the samples showed two chemical states of carbon. For the annealed samples, there was an additional shoulder at higher binding energies that increased the percentage of carbon on the surface. With respect to the Li 1s region, all the samples showed one peak at 55 eV (see Figure S2b).

Table 2: Surface composition of LVO samples quantified from XPS peaks and percentage of carbon at the surface of them. The Open Circuit Voltage (OCV) in Volts was measured during the electrochemical experiments and the thickness (in nm) of each film was measured by ellipsometry.

	LVO 90W T25	LVO 90W T300	LVO 120W T25	LVO 120W T300
Surface Composition	$\text{Li}_{4.2}\text{V}_{2.0}\text{O}_{5.3}$	$\text{Li}_{3.0}\text{V}_{2.0}\text{O}_{5.3}$	$\text{Li}_{4.3}\text{V}_{2.0}\text{O}_{5.7}$	$\text{Li}_{5.4}\text{V}_{2.0}\text{O}_{6.2}$
Composition with Li_2CO_3 discounted	$\text{Li}_{3.2}\text{V}_{2.0}\text{O}_{3.9}$	$\text{Li}_{1.6}\text{V}_{2.0}\text{O}_{3.0}$	$\text{Li}_{3.9}\text{V}_{2.0}\text{O}_{5.1}$	$\text{Li}_{5.0}\text{V}_{2.0}\text{O}_{5.5}$
Carbon concentration (at %)	6.3	17	4.2	8.1
Open Circuit Voltage (V vs Li)	3.26	3.42	2.46	3.16
Thickness (nm)	280	225	506	232

The surface composition of each film is presented in Table 2. The LVO 90W T25 and T300 films showed a similar V:O ratio, with a slight excess of oxygen. LVO 120W T25 and T300 samples have more oxygen and lithium on their surfaces, which indicates that they might have a significant quantity of lithium carbonate at their surfaces. Using the carbon amount calculated from the peak at 286 eV, we subtracted the lithium carbonate contribution from the surface composition, shown in Table 2. The LVO 120 W samples still show a very high amount of lithium at the surface and a composition closer to V_2O_5 . The LVO 90W samples, however, had a smaller amount of lithium and significant oxygen deficiency. This may be explained by a reduced amount of O released from the Li_2O at lower power, and indicates that supplemental O_2 may be needed in the sputtering atmosphere for this case. An XPS depth profile done using a 100 nm thick LVO 90W T300 sample showed that a portion of the lithium had diffused to the surface of the film and to the substrate/film interface. This result is shown in Figure 3. There was a non-uniform lithium composition throughout the film thickness with a depth average composition of 1.7 mols of lithium, which agrees with the composition calculated by discounting the amount of lithium carbonate and with the

conclusions from the Raman spectra about the coexistence of different lithiated phases in the LVO samples. There was a negligible carbon concentration throughout the film and a carbon segregation at the surface (approximately 20 %), possibly due to the cooling effect after annealing, and at the bottom Au surface, which was air exposed prior to the LVO deposition. The oxygen concentration followed the same trend as the vanadium content.

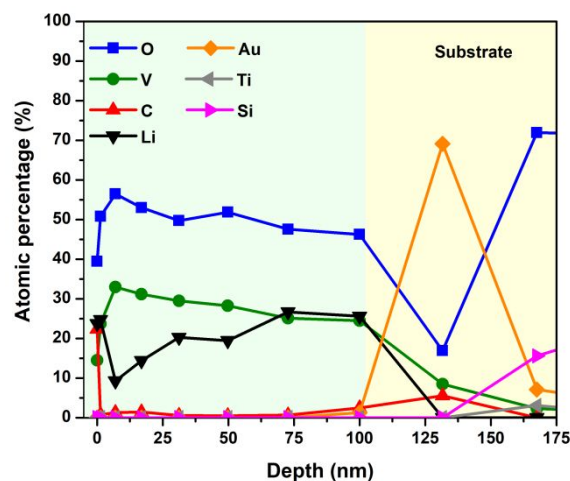


Figure 3: Relative composition of LVO 90W T300 100 nm thick sample as a function of depth. The composition was calculated from a XPS depth profile analysis. The Si substrate was coated with 500 nm of SiO_2 , an adhesion layer of Ti and 50 nm of Au.

Figure 4 presents the spectra for the O 1s and V 2p region. Because of the proximity of their binding energies, a single background was used. There is a doublet of the V 2p peak due to its spin-orbit splitting, and the relative intensity of the peaks in this doublet is related to their degeneracy. There are two contributions to the V 2p signal, which correspond to different oxidation states. The larger peak is associated with V^{5+} oxidation state, at higher binding energies, while the peak corresponding to the V^{4+} state is located at lower binding energies. The positions of the V^{5+} and V^{4+} peaks did not vary for different LVO samples, but their relative intensities were changed. The contribution of V^{4+} oxidation state is significantly bigger in LVO 90W T300 sample than for LVO 90W T25.

The surface of the LVO 120W T25 film was similar to the surface of LVO 90W T25, indicating that there are the same V oxidation states as in the less lithiated sample, despite the increase in distortion of the V-O layers seen in Raman (Figure 2). For the LVO 120W samples (with and without a post-anneal step), a new peak in the O 1s region is observed. Since there are more lithium ions in these samples, this could be unrelated to the LVO structure, and indicative of the formation of lithium carbonate (Li_2CO_3) or excess Li_2O at the surface since its O 1s binding energy is at 532 eV.⁴⁵ The LVO 120W T300 sample presented only a small contribution of the V^{4+} oxidation state on the surface which is unexpected given the large amount of Li at the surface. One possible explanation for that could be that the excess of lithium in this LVO sample, after the annealing step, diffuses more to the surface and bonds with the oxygen;

hence, a considerable fraction of lithium ions that should have been between the vanadium oxide layers forms Li_2CO_3 , so the V^{5+} state is more predominant than the V^{4+} at the surface in this case.

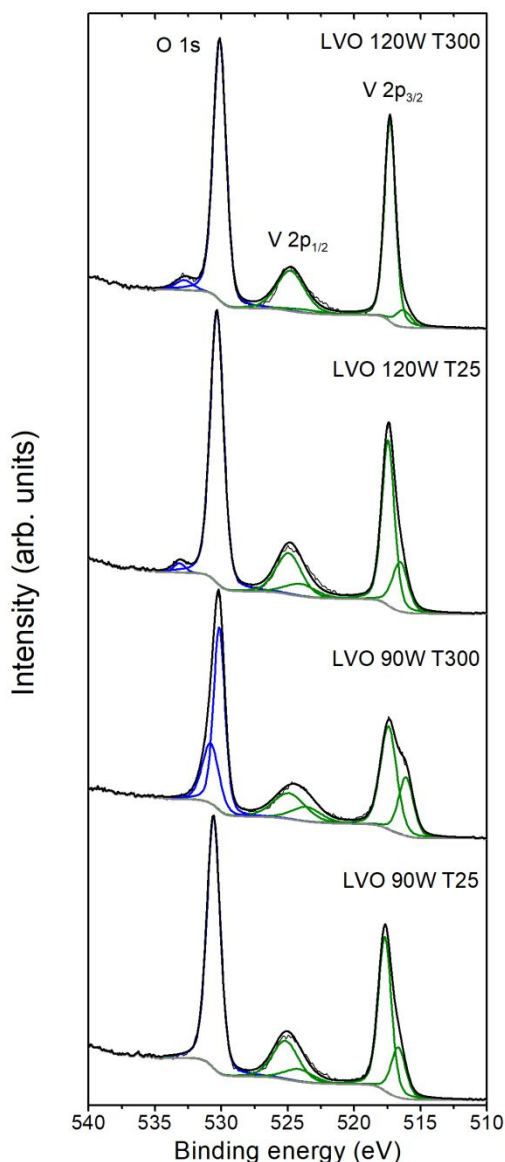


Figure 4: High-resolution X-Ray Photoelectron Spectroscopy of LVO samples showing the O 1s and V 2p region. The blue and green peaks correspond to oxygen 1s and vanadium 2p peaks, respectively. An XPS spectra from the V_2O_5 sample surface is shown in Figure S1 from Supplementary Information for comparison.

Electrochemistry. For the four different LVO samples, the electrochemistry was evaluated by doing cyclic voltammetry (CV) and galvanostatic charge/discharge measurements in a beaker cell versus Li foil. The deposition time of the samples was the same, but since the rate and density varied with sputtering conditions, the film thicknesses are not equivalent. In addition, a 200 nm thick V_2O_5 film was also electrochemically cycled. The open circuit voltage (OCV) of each film, presented in Table 2, agrees qualitatively with the sputtering conditions: the higher the used lithium oxide target power, the bigger the amount of lithium in the sample, which lowers the OCV. A post-anneal step

may have allowed a fraction of lithium ions to diffuse to the surface of the films, so the lithium content in the bulk is smaller in the post-annealed samples, and therefore their OCV is higher. The V_2O_5 film in this work presented an OCV of 3.4 V vs Li/Li^+ , which is the voltage of the un lithiated state.

The OCVs measured in each LVO sample are higher than expected. From the XPS surface measurements, we would expect to see OCVs below 3.0 V for every LVO sample. In particular, LVO 90W T300 has the same OCV as the $\alpha\text{-V}_2\text{O}_5$ sample, even though both the Raman and the XPS results had confirmed that this sample has lithium inside it. Interestingly, the OCV follows the same trend as the oxygen deficiency level found on their composition after subtracting the contribution due to lithium carbonate (see Table 2). LVO 120W T25 showed the closest composition to V_2O_5 , having the lowest OCV. LVO 90W T300 sample was the most oxygen deficient one, and its OCV is the highest found on this set of samples. From computational simulation of lithiation process in V_2O_5 , it is known that oxygen vacancies play a critical role in lithium-ion diffusion.⁴⁶ Depending on the oxygen site in the crystal structure, an oxygen vacancy can increase the activation energy of lithium-ion diffusion, which reduces the usable capacity of the material during cycling. LVO 90W T300 had the same amount of lithium inserted as the LVO 90W T25 sample, thus the post-annealing also contributed to the formation of unfavorable oxygen vacancies. Hence, the surface chemistry of the samples was different, especially with respect to the amount of oxygen vacancies, depending on the lithium oxide amount using during deposition and the thermal treatment. An important difference, though, is the voltage of the electrochemical reactions. As we will see below, for the V_2O_5 film the initial OCV is near the highest voltage of the electrochemical reactions, whereas for the LVO 90W T300 film, the initial OCV is actually below the voltage of the electrochemical reactions, which shows that Li is saturated in the film.

It is important to emphasize that, for these experiments, the electrochemical cycling began by charging the cell up to 4.0 V to evaluate the extraction of lithium ions inserted in the co-sputtering process. The samples were cycled under a constant scan rate between 4.0 V and 2.6 V vs Li/Li^+ , and then galvanostatic charge-discharge cycles were performed in the one lithium insertion voltage window (2.6-4.0 V), as seen in Figure 5. Two redox peaks were found at 3.2 and 3.4 V for the V_2O_5 sample, with corresponding plateaus that were observed in the galvanostatic charge/discharge curves (Figure 5 a and b). The capacity reached 109 mAh/g, which corresponds to 74 % of the maximum theoretical capacity for one lithium insertion. A possible cause for this capacity loss is the annealing temperature of 300 °C: even though it is possible to form $\alpha\text{-V}_2\text{O}_5$, as the Raman spectra has shown, the degree of crystallinity may not be very high. A V_2O_5 film annealed at 500 °C provides a capacity closer to the maximum theoretical as it is shown in Fig. S3, but here the V_2O_5 film at 300 °C is used for comparison with the LVO samples.

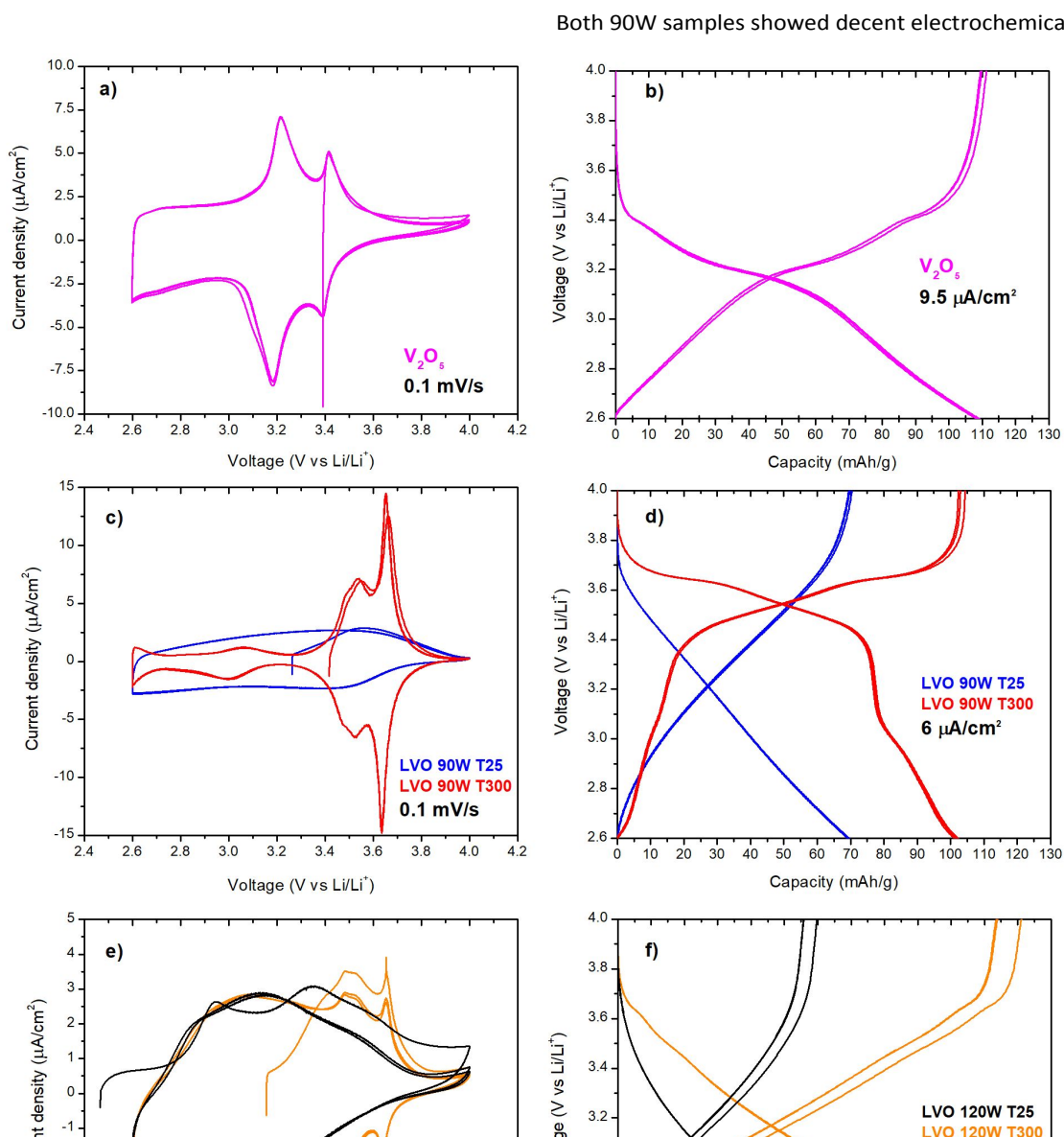


Figure 5: Cyclic voltammetry (CV) and galvanostatic charge/discharge measurements for one lithium insertion. a) CV and b) galvanostatic charge/discharge curves of 200 nm thick V_2O_5 film, c) CV of LVO 90W T25 (blue) and LVO 90W T300 (red), d) galvanostatic charge/discharge curves of LVO 90W T25 (blue) and LVO 90W T300 (red), e) CV of LVO 120W T25 (black) and LVO 120W T300 (orange), f) galvanostatic charge/discharge curves of LVO 120W T25 (black) and LVO 120W T300 (orange). Three cycles of charge/discharge were done for all the electrochemical measurements showed above and then three galvanostatic charge/discharge measurements were done immediately after the CV cycles.

Both 90W samples showed decent electrochemical activity and

good reversibility. For the LVO 120W samples (Figure 5 e and f) there is a drop in the oxidative current after the first cycle, but otherwise they show excellent stability. Except for the LVO 90W T300 sample, the other LVO samples exhibit broad peaks in CV and a continual slope in galvanostatic charge/discharge curves, which is characteristic of a pseudocapacitive behavior. Those broad peaks were stable under different scan rates as shown in

Figure S4 for LVO 90W T25. The unannealed samples showed a smaller capacity in comparison to the post-annealed ones. The LVO 90W T25 sample had a discharge capacity of 70 mAh/g, while the LVO 90W T300 film showed a discharge capacity of 101 mAh/g. Also, the LVO 120W T25 sample showed a capacity of 55 mAh/g, and the LVO 120W T300 film showed a discharge capacity of 114 mAh/g. The post-annealed samples showed two sharp redox peaks at 3.52 and 3.64 V, which is a higher voltage than the V_2O_5 film in this work and higher than electrochemically lithiated V_2O_5 reported elsewhere.^{42,47}

The LVO 90W T300 sample has the most interesting electrochemical results. From Figure 5c, it is possible to see that there is an additional small redox peak located between 3.0 and 3.1 V for both charge and discharge, which could be from either a lithiation of another vanadium oxide polymorph or an intermediate phase transformation of $Li_xV_2O_5$ that may have occurred. The phase changes can be confirmed by the plateaus observed in the galvanostatic charge/discharge curves (Figure 5d), for both charge and discharge processes. The LVO 90W T300 sample's discharge capacity is 93 % of the capacity from the sputtered V_2O_5 film. The LVO 120W T300 film showed a capacity 104.6 % that of the V_2O_5 sample. One hypothesis for this unique behavior of the LVO 90W T300 sample in terms of sharp electrochemical peaks and chemical composition from the XPS is that the inserted lithium ions occupy the expected sites in a lithiated vanadium oxide sample between the V-O layers due to the diffusion of them during the post-annealing step, while for the unannealed sample the lithium ions may be occupying different sites that do not bound so well with the oxygen.⁴⁶

A similar study was done for the two-lithium insertion window, shown in Figure 6. For this large voltage window, the same samples were used. After the final discharge cycle obtained in Figure 5, the LVO films were at a voltage of 2.6 V and were then cycled up to 4.0 V with a constant scan rate (CV). Hence, the samples had one lithium inserted at the beginning of this second electrochemical study. For the V_2O_5 sample, a duplicate film, obtained from the same batch, was first cycled in the one lithium voltage window. Then, the galvanostatic charge/discharge cycles were performed starting at 2.6 V for the two-lithium voltage window and stopped at the discharged state. Following that experiment, a CV was done starting at 2.0 V. This sample still has the two redox peaks corresponding to one lithium insertion at 3.2 and 3.4 V, but they are much less pronounced in this two-lithium insertion window (Figure 6a). In addition, the pseudocapacitive current is much larger than before, and it is possible to see an additional oxidation peak at 2.65 V, and two reduction peaks at 2.5 and 2.3 V. The capacity, after the first charge/discharge cycle in this two-lithium window (Figure 6b), was 273 mAh/g, which corresponds to 93 % of the maximum theoretical capacity for V_2O_5 in this voltage window. It is still unknown why the relative capacity with respect to the theoretical one is lower for one lithium insertion than for two lithium insertion for the same sample.

The LVO 90W T25 sample, represented by the blue curves, showed good stability in this larger voltage window with no observed capacity drop through the charge/discharge cycles

(Figure 6d). The capacity, however, is still very low in comparison to the V_2O_5 film. The LVO 90W T300 sample showed much less stability in this large voltage window: the current density was high during the first cycle, reaching up to 20 $\mu\text{A}/\text{cm}^2$, but peak currents were reduced for the subsequent cycles. This sample also showed two sharp redox peaks corresponding to the second lithium insertion/extraction at 2.35 and 2.48 V (Figure 6c). There is a capacity loss during two lithium insertion that was reproducible, as shown in Figures S5 and S6. A new LVO 90W T300 sample was produced and its galvanostatic charge/discharge curves were taken in the two-lithium insertion window without any previous cycling. It was possible to observe the plateaus of phase changes for every cycle, but there was also a capacity loss of 48 % between the first and the third cycle in this case.

For the LVO 120W T25 and T300 samples, the reversibility and the capacitive behavior remained even for the extended voltage window down to 2.0 V (Figure 6e). The additional two redox peaks located at 2.35 and 2.48 V observed in LVO 90W T300 also appeared in the LVO 120W T300 sample and an oxidation peak appeared between 2.8 and 2.9 V for both LVO 120W T25 and T300 films. The shape of the galvanostatic charge/discharge curves indicates that, for these highly lithiated samples, there was a phase transition before inserting the second lithium ion that was reversible. In addition, there was a small capacity drop after the first charge/discharge cycle, with a capacity of 95 mAh/g and 222 mAh/g for LVO 120W T25 and LVO 120W T300, respectively (Figure 6f). In comparison to the V_2O_5 , the LVO 120W T300 film reached 81 % of its theoretical capacity.

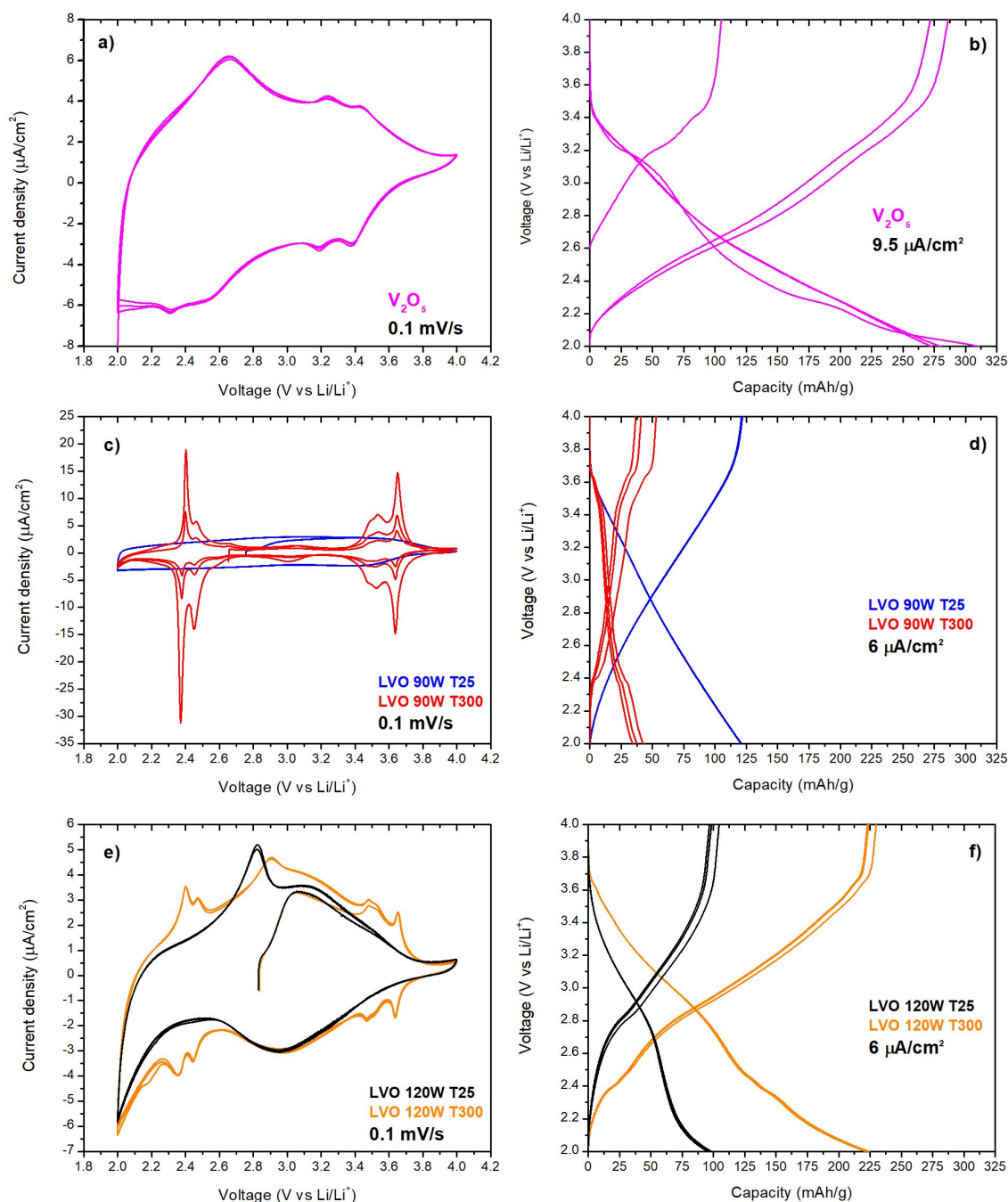


Figure 6: Cyclic voltammetry (CV) and galvanostatic charge/discharge cycles for two lithium insertion. a) CV and b) galvanostatic charge/discharge curves of 200 nm thick V_2O_5 film, c) CV of LVO 90W T25 (blue) and LVO 90W T300 (red), d) galvanostatic charge/discharge curves of LVO 90W T25 (blue) and LVO 90W T300 (red), e) CV of LVO 120W T25 (black) and LVO 120W T300 (orange), f) galvanostatic charge/discharge curves of LVO 120W T25 (black) and LVO 120W T300 (orange).

Post-cycling surface analysis in the two Li voltage window. The capacity fading observed for LVO 90W T300 sample after electrochemical cycling from 2.0 V to 4.0 V was unexpected, given its sharp peaks in CV and good Raman intensity. In order to understand this, Raman and XPS surface analysis were performed on this film, and compared with the LVO 90W T25 sample which was much more stable under electrochemical cycling. For this the samples were removed from the liquid electrolyte, rinsed in propylene carbonate, and dried soon after

the end of the cycling shown in Figure 6d, after they had reached 2.0 V vs Li.

Raman spectroscopy agrees in large part with the electrochemical data from Figures 5 and 6 in that the LVO 90W T25 sample appears deeply lithiated, while there has been little change in the LVO 90W T300 sample. In Figure 7a, we see the LVO 90W T25 sample has its structure modified after lithium ions are inserted, as evidenced by the appearance of different vibrational modes after cycling (spectrum II) in comparison to the as-deposited film (spectrum I). It is expected that a broader

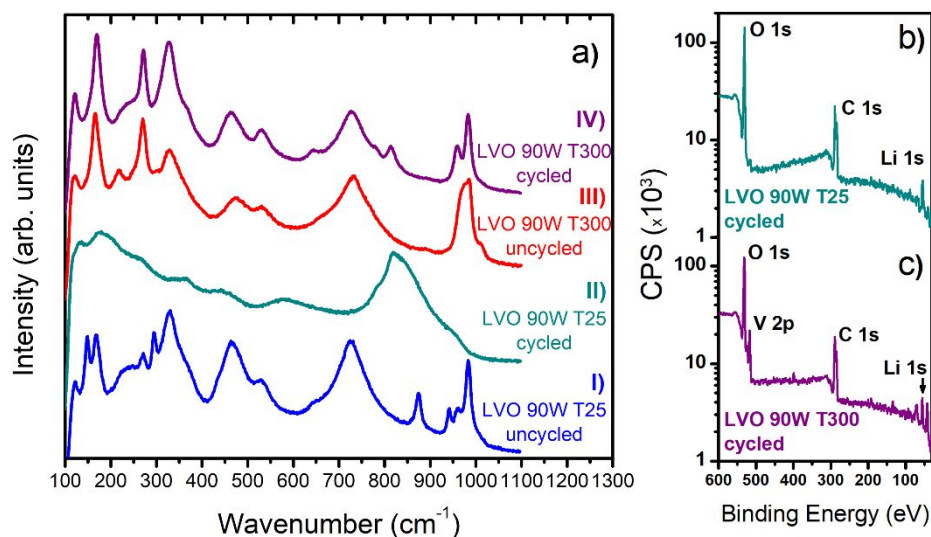


Figure 7: Raman spectra and XPS of uncycled (as deposited) and cycled samples (analyzed at a discharged state of 2.0 V vs Li). a) Raman spectra of LVO 90W T25 I) before cycling (blue) and II) after cycling (dark cyan), and LVO 90W T300 III) before cycling (red), and IV) after cycling (purple). b) XPS of LVO 90W T25 surface and c) XPS of LVO 90W T300 surface, both after cycling. Samples were cleaned after electrochemical testing to remove residual electrolyte from the surface.

Raman peak appears in the 700 – 1000 cm^{-1} range when V_2O_5 has two lithium ions intercalated in its structure.⁴³ In contrast, the LVO 90W T300 sample showed very similar Raman spectra before (III) and after (IV) cycling. The LVO 90W T300 sample showed an attenuation of a peak at 230 cm^{-1} after cycling and small peaks are seen at 360 cm^{-1} , 650 cm^{-1} , 800 cm^{-1} and 815 cm^{-1} . Those small differences correspond to V-O vibration modes from individual layers as previously described in the Raman section, which may indicate that some structural change occurred after cycling. Different lattice distortions yield to new vibration modes, which can affect the diffusion lithium path and the capacity retention of the material. On the other hand, the sharp Raman signal from the LVO 90W T300 samples is interesting, because it indicates a large amount of the as-deposited LVO film is intact, despite the drop in capacity seen in Figure 6c and d.

The XPS surface spectra corroborate the Raman results as well, showing deep lithiation of the LVO 90W T25 sample and that the structure of the LVO 90W T300 film is intact. In Figure 7b, XPS only shows Li_2CO_3 at the surface of the LVO 90W T25 sample, which is to be expected because the sample was exposed to air after electrochemical cycling, prior to XPS. The complete coverage by Li_2CO_3 , combined with the structural changes observed in Raman and electrochemical capacity, all indicate a high degree of lithiation. For the LVO 90W T300 sample, the chemical composition of its surface presented in Figure 7c shows a strong V 2p doublet besides the oxygen and lithium peak, which implies much less coverage by Li_2CO_3 than the LVO 90W T25 film. This XPS result is similar to the as-deposited state, though with more C contamination (likely from the cleaning process, rather than electrolyte, as no Cl is detected). The lack of any visible Au or Si peaks (from the substrate) implies that the film is still contiguous. While more study is warranted, it seems that the decrease in capacity in the LVO 90W T300 film may be related to its oxygen deficiency

and/or the formation of a thick SEI, though why that is only observed for these samples and not others remains unknown.

Solid-state battery prototype. The LVO 120W T300 was the chosen condition to use LVO as a cathode material for thin-film SSBs. The main objective on this part of the study was to prove that the lithiation provided during the co-sputtering would enable electrochemically active solid-state devices using a lithium-free anode. We were able to produce SSBs and cycle them, although the voltage window and therefore the energy density are low, along with the discharge capacity. LiPON was used as the solid electrolyte, while amorphous silicon was deposited as the anode. Au is the cathode current collector and Cu is the anode current collector. All the depositions were done in the same sputter chamber and with no air exposure between any layers.

From Figure 8a, cross-sectional SEM image shows that the interfaces are smooth, with a total device thickness of less than 1.2 μm . EDS revealed that there is no distinction between the amorphous silicon and copper layers, which indicates that there is possibly intermixing at the anode side during annealing. Cyclic voltammetry was done to evaluate the working voltage window of the devices as shown in Figure 8b. Unfortunately, it was not possible to increase the voltage higher than 1.5 V (vs Si) without causing soft shorting, and a high current, so the measurements were taken up to this value.

The lower voltage limit was set to the point at which no redox peaks were observed. Since the Si is acting as the voltage reference, it is important to note that the anode and cathode are not capacity matched (the Si anode is too thick). Amorphous Si typically reacts between 0.1 and 3 V vs Li ,⁴⁸⁻⁵⁰ but the Si is likely not reaching 0.1 V vs Li when lithiated. In an extreme case, our Si anode may only be cycling between 2 and 3 V vs Li, which means that a very small fraction of lithium ions is inserted in the silicon layer. Therefore, we expect the lower voltage cut off to place the LVO cathode at 2 V vs Li, and the upper cut off to

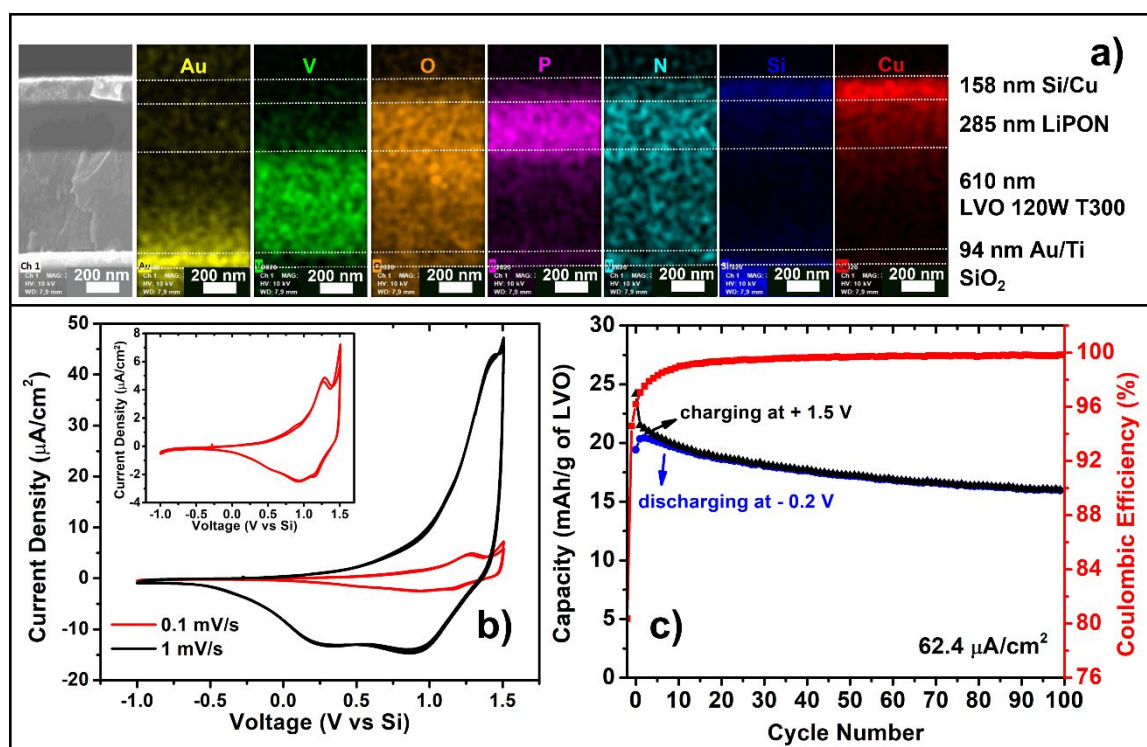


Figure 8: a) SEM cross-sectional image and EDS spectra of an as-deposited thin-film solid-state device using LVO as the cathode, LiPON as electrolyte and amorphous silicon as the anode. b) Cyclic voltammetry of solid-state device using different scan rates of 1 (black curve) and 0.1 (red curve) mV/s. The inset image provides a zoom in of the voltammogram at 0.1 mV/s. Three cycles were done for each scan rate. c) Capacity and coulombic efficiency of the solid-state battery as a function of cycle number. The analysis was done using a current density of $62.4 \mu\text{A}/\text{cm}^2$, which corresponds to a C-rate of 22C.

correspond to between 2.1–3.5 V, depending on the exact lithiation state of the Si anode.

From Figure 8b, there are two broad reduction peaks at 0.25 and 0.9 V and a small oxidation peak at 1.4 V under a scan rate of 1 mV/s. Under a 10 times slower scan rate, the broad peak at 0.9 V seemed to be made of two peaks at 0.93 and 1.17 V while the peak at 0.25 shifted to 0.5 V. The oxidation peak is more pronounced in this slower scan rate, and it shifted to 1.25 V. Also, there is a small and broad oxidation peak at 0.92 V that was not visible at faster scan rates.

The thin-film SSB was cycled at a constant current density to evaluate its performance for fast charging and discharging, as shown in Figure 8c. The discharge capacity is not high, starting from 20 mAh/g and decreasing to 16 mAh/g after 100 cycles. The lower capacity than expected can be attributed to a set of factors, including the lower voltage window, the quality of the anode/current collector layers, the excess of silicon for this amount of charge provided by the LVO layer and possible lithium trapping sites on the interfaces. A 20 % of capacity fading was observed from the beginning to the end of cycling under a fast C-rate (22C). In addition, the coulombic efficiency was very stable after the first 20 cycles, reaching 99.8 % of efficiency at the 100th cycle. Slower charge/discharge rates were also tested for a reduced number of cycles, and the capacity presented the same order of magnitude as cycling under faster rates (see Figure S8). The solid-state device was not able to store as large an amount of charge as it was expected from the electrochemistry observed in Figures 5 and 6.

However, the SSB demonstrated that lithium-ions provided only by the co-sputtering deposition can be transported under this device configuration.

General Discussion

The co-sputtering procedure was confirmed as a very promising fabrication process of pre-lithiated vanadium oxide film. The independent control of the parameters of Li_2O and V_2O_5 targets enabled the development of LVO samples with different amounts of lithium concentration, at least to the composition LiV_2O_5 as confirmed by XPS and OCV measurements, with distinct electrochemical behaviors.

The Raman spectroscopy showed that characteristic peaks from the $\alpha\text{-V}_2\text{O}_5$ were found in the LVO films, but with more vibrational modes. In general, unannealed samples showed more Raman peaks in comparison to annealed samples, which can be interpreted as a greater diversity of crystal structures when there is no heat treatment step. Also, the high number of peaks between 940 and 1000 cm^{-1} indicate that the LVO samples have different lithium concentrations.

The low surface reactivity found for the LVO 90W T300 sample on XPS analysis was confirmed by the unique electrochemical behavior in a two-lithium insertion window, where the capacity was drastically reduced when further cycled with its structure mostly preserved, probably due to its intrinsic oxygen deficient structure in comparison to the other studied samples. The unannealed films showed an inferior

electrochemical activity with respect to capacity that could be ascribed by the lower ordering in LVO structure. The post-annealed films showed the same electrochemical peaks for both one lithium and two lithium insertion windows. The redox peaks for one lithium insertion, in particular, occurred at a higher voltage than the V_2O_5 film, thus the LVO samples can provide a higher energy density. The LVO 120W T300 film reached 81 % of the capacity of an electrochemically lithiated V_2O_5 film with similar thickness for both one and two Li insertion windows.

This result confirms the success of the co-sputtering process as an effective way to pre-lithiate a cathode material without exposing the device to deleterious conditions, i.e., the procedure is suitable for use in a continuous UHV process like a thin-film solid-state battery involving only dry or vacuum based processes. Continuous UHV processing is required for advanced 3D architectures such as multilayered stacks in which the energy and power density of the device can be increased without compromising the electrochemical activity of the electrodes.

There have been other approaches in the literature to deposit thin film lithiated electrodes involving other materials. Lithium cobalt oxide and lithium manganese oxide are common materials that were also deposited by rf-sputtering. Although they can theoretically provide decent capacity at higher voltages, they require a high degree of crystallinity that can be achieved using heat treatments such as rapid thermal annealing with temperatures greater than 500 °C and plasma irradiation.⁵¹⁻⁵⁶ Those treatments, unfortunately, cause film cracks and voids besides losing the control of the desired lithium composition.⁵¹ From a perspective of building a solid-state battery, those procedures would be inappropriate since internal short circuits could result from the cracks and high temperatures may affect the subsequent deposited materials (the solid electrolyte, the anode and the current collector). Therefore, the development of the co-sputtered LVO as a dry-method to lithiate vanadium oxide, using relatively low temperatures during annealing, served as a motivation to build thin-film solid-state batteries. Applications in microelectronics require faster charge and discharge rates combined with miniaturization of devices, so improvements can be done on the fabricated devices to achieve better capacity with faster charging.

Conclusions

In this work, a new route to develop pre-lithiated cathode materials by co-sputtering was demonstrated. In this process, films with different lithium concentration can be manufactured in a simple way using two targets that are sputtered at the same time. One major benefit of this process is the ability of fabricating a cathode material in a complete dry process that has a sufficient electrochemical activity to be used in solid-state devices. Raman spectroscopy showed additional vibrational modes in LVO samples that are not present in α - V_2O_5 , specially for higher wavenumbers, indicating LVO films with multiple lithiated phases. This is further evidenced in XPS depth profiling,

which showed the lithium concentration is not uniform in the depth of the film.

As a consequence of such a structure that accommodates lithium ions in presumably different chemical surroundings, an interesting electrochemical behavior is observed. LVO samples that did not have any post-annealing step showed a stable capacitive behavior, while LVO films post-annealed at 300 °C presented well-defined redox peaks for both one lithium and two lithium insertion windows. The best electrochemical performance was obtained for a film with high lithium content and modest post annealing (LVO 120W T300), which had the largest, stable capacity under cycling. Using this set of conditions to lithiate a cathode layer from the deposition step, a thin-film solid-state battery prototype was fabricated and electrochemically tested. The capacity is lower than expected, involving a 20 % capacity loss over 100 cycles under a faster C-rate (22C) with near 100 % coulombic efficiency. Therefore, this process can effectively fabricate pre-lithiated cathode materials, such as lithiated vanadium oxide, but not limited to it, that are electrochemically active for solid-state lithium-ion batteries. The co-sputtering process can be further explored to fabricate different cathode materials for Na and Mg-ion solid-state batteries.

Author Contributions

V.C.F. and D.M.S. planned the research. D.M.S., S.B.L. and G.W.R. developed the concepts. V.C.F. wrote the manuscript, fabricated the samples and conducted the Raman characterization. D.M.S. assisted V.C.F. with the XPS characterization. N.S.K. conducted the experimental setup of electrochemical techniques. N.S.K. and D.M.S. contributed with discussions during the process of writing the manuscript. All authors have given approval to the final version of the manuscript.

Conflicts of interest

There are no conflicts to declare.

Acknowledgements

We acknowledge the help of Dr. Zoey Warecki for SEM and EDS data acquisition. This work was initially supported by the University of Maryland's Medical Device Development Fund. Part of this work, particularly the pursuit of architectures which stack up multiple planar thin film batteries, was supported by the U.S. Department of Energy, Office of Science, Office of Basic Energy Sciences, under Grant DE-SC0021070. We acknowledge the support of the Maryland NanoCenter and its FabLab.

References

- 1 D.H.S. Tan, A. Banerjee, Z. Chen, Y.S. Meng, *Nature Nanotechnology*, 2020, **15** (3), 170–180.
- 2 J.G. Kim, B. Son, S. Mukherjee, N. Schuppert, A. Bates, O. Kwon, M.J. Choi, H.Y. Chung, S. Park, *Journal of Power Sources*, 2015, **282**, 299–322.
- 3 A. Manthiram, X. Yu, S. Wang, *Nature Reviews Materials*, 2017, **2** (4), 1–16.
- 4 Y. Wang, B. Liu, Q. Li, S. Cartmell, S. Ferrara, Z.D. Deng, J. Xiao, *Journal of Power Sources*, 2015, **286**, 330–345.
- 5 S. Lobe, A. Bauer, S. Uhlenbruck, D. Fattakhova-Rohlfing, *Advanced Science*, 2021, 2002044.
- 6 G.E. Blomgren, *Journal of The Electrochemical Society*, 2017, **164** (1), A5019–A5025.
- 7 J.B. Bates, N.J. Dudney, B. Neudecker, A. Ueda, C.D. Evans, *Solid State Ionics*, 2000, **135**, 33–45.
- 8 S. Randau, D.A. Weber, O. Kötz, R. Koerver, P. Braun, A. Weber, E. Ivers-Tiffée, T. Adermann, J. Kulisch, W.G. Zeier, F.H. Richter, J. Janek, *Nature Energy*, 2020, **5** (3), 259–270.
- 9 G.W. Rubloff, A.C. Kozen, S. Bok Lee, *Journal of Vacuum Science & Technology A: Vacuum, Surfaces, and Films*, 2013, **31** (5), 058503.
- 10 M. Noked, C. Liu, J. Hu, K. Gregorczyk, G.W. Rubloff, S.B. Lee, *Accounts of Chemical Research*, 2016, **49** (10), 2336–2346.
- 11 N.J. Dudney, *ECS Interface*, 2008, **17**, 44–48.
- 12 J. Xie, Y.C. Lu, *Nature Communications*, 2020, **11** (1), 1–4.
- 13 H. Zhang, H. Ning, J. Busbee, Z. Shen, C. Kiggins, Y. Hua, J. Eaves, J. Davis III, T. Shi, Y.T. Shao, J.M. Zuo, X. Hong, Y. Chan, S. Wang, P. Wang, P. Sun, S. Xu, J. Liu, P.V. Braun, *Science Advances*, 2017, **3**(5), e1602427.
- 14 D. McNulty, D.N. Buckley, C. O'Dwyer, *Journal of Power Sources*, 2014, **267**, 831–873.
- 15 Q. Liu, Z.F. Li, Y. Liu, H. Zhang, Y. Ren, C.J. Sun, W. Lu, Y. Zhou, L. Stanciu, E.A. Stach, J. Xie, *Nature Communications*, 2015, **6**(1), 1–10.
- 16 Y. Zhang, J. Lai, Y. Gong, Y. Hu, J. Liu, C. Sun, Z.L. Wang, *ACS Applied materials & interfaces*, 2016, **8**(50), 34309–34316.
- 17 Y. Yue, H. Liang, *Advanced Energy Materials*, 2017, **7** (17), 1602545.
- 18 H. Song, C. Zhang, Y. Liu, C. Liu, X. Nan, G. Cao, *Journal of Power Sources*, 2015, **294**, 1–7.
- 19 H. Song, C. Liu, C. Zhang, G. Cao, *Nano Energy*, 2016, **22**, 1–10.
- 20 B. Yan, X. Li, Z. Bai, Y. Zhao, L. Dong, X. Song, D. Li, C. Langford, X. Sun, *Nano Energy*, 2016, **24**, 32–44.
- 21 C.F. Armer, M. Lübke, M.V. Reddy, J.A. Darr, X. Li, A. Lowe, *Journal of Power Sources*, 2017, **353**, 40–50.
- 22 M. Kurttepel, S. Deng, F. Mattelaer, D.J. Cott, P. Vereecken, J. Dendooven, C. Detavernier, S. Bals, *ACS Applied Materials and Interfaces*, 2017, **9** (9), 8055–8064.
- 23 S. Koike, T. Fujieda, T. Sakai, S. Higuchi, *Journal of Power Sources*, 1999, **81–82**, 581–584.
- 24 N. Kumagai, H. Kitamoto, M. Baba, S. Durand-Vidal, D. Devilliers, H. Groult, *Journal of Applied Electrochemistry*, 1998, **28** (1), 41–48.
- 25 M.S.B. De Castro, C.L. Ferreira, R.R. De Avillez, *Infrared Physics and Technology*, 2013, **60**, 103–107.
- 26 E. Brown, J. Acharya, G.P. Pandey, J. Wu, J. Li, *Advanced Materials Interfaces*, 2016, **3** (23), 1600824.
- 27 R. Pfenninger, M. Struzik, I. Garbayo, E. Stilp, J.L.M. Rupp, *Nature Energy*, 2019, **4**, 475–483.
- 28 M. Rawlence, A.N. Filippin, A. Wackerlin, T.Y. Lin, E. Cuervo-Reyes, A. Remhof, C. Battaglia, J.L.M. Rupp, S. Buecheler, *ACS Appl. Mater. Interfaces*, 2018, **10**, 13720–13728.
- 29 J. Sastre, A. Priebe, M. Dobeli, J. Michler, A. Tiwari, Y.E. Romanyuk, *Adv. Mater. Interfaces*, 2020, **7**, 2000425.
- 30 C.F. Xiao, J.H. Kim, D. Choi, Y.C. Park, J.H. Kim, J. Park, Y.J. Kim, H.S. Kim, *Journal of Alloys and Compounds*, 2019, **801**, 550–557.
- 31 S. Kanazawa, T. Baba, K. Yoneda, M. Mizuhata, I. Kanno, *Thin Solid Films*, 2020, **697** (June 2019), 137840.
- 32 R. Baddour-Hadjean, C. Navone, J.P. Pereira-Ramos, *Electrochimica Acta*, 2009, **54** (26), 6674–6679.
- 33 C. Delmas, H. Cognac-Auradou, J.M. Cocciantelli, M. Ménétrier, J.P. Doumerc, *Solid State Ionics*, 1994, **69** (3–4), 257–264.
- 34 Y. Wang, K. Takahashi, K. Lee, G. Cao, *Advanced Functional Materials*, 2006, **16** (9), 1133–1144.
- 35 S.H. Lee, H.M. Cheong, M. Je Seong, P. Liu, C.E. Tracy, A. Mascarenhas, J.R. Pitts, S.K. Deb, *Journal of Applied Physics*, 2002, **92** (4), 1893–1897.
- 36 S.H. Lee, H.M. Cheong, M.J. Seong, P. Liu, C.E. Tracy, A. Mascarenhas, J.R. Pitts, S.K. Deb, *Solid State Ionics*, 2003, **165** (1–4), 111–116.
- 37 R. Baddour-Hadjean, J.P. Pereira-Ramos, C. Navone, M. Smirnov, *Chemistry of Materials*, 2008, **20** (5), 1916–1923.
- 38 C. Zhang, Q. Yang, C. Koughia, F. Ye, M. Sanayei, S.J. Wen, S. Kasap, *Thin Solid Films*, 2016, **620**, 64–69.
- 39 H.C. Ho, Y.C. Lai, K. Chen, T.D. Dao, C.H. Hsueh, T. Nagao, *Applied Surface Science*, 2019, **495** (July), 143436.
- 40 R. Baddour-Hadjean, E. Raekelboom, J.P. Pereira-Ramos, *Chemistry of Materials*, 2006, **18** (15), 3548–3556.
- 41 R. Baddour-Hadjean, V. Golabkan, J.P. Pereira-Ramos, A. Mantoux, D. Lincot, *Journal of Raman Spectroscopy*, 2002, **33** (8), 631–638.
- 42 H. Jung, K. Gerasopoulos, A.A. Talin, R. Ghodssi, *Electrochimica Acta*, 2017, **242**, 227–239.
- 43 A. Jarry, M. Walker, S. Theodoru, L.J. Brillson, G.W. Rubloff, *Chemistry of Materials*, 2020, **32** (17), 7226–7236.
- 44 R. Baddour-Hadjean, A. Marzouk, J.P. Pereira-Ramos, *Journal of Raman Spectroscopy*, 2012, **43** (1), 153–160.
- 45 A.C. Kozen, A.J. Pearse, C.F. Lin, M.A. Schroeder, M. Noked, S.B. Lee, G.W. Rubloff, *Journal of Physical Chemistry C*, 2014, **118** (48), 27749–27753.
- 46 W.Y. Ma, B. Zhou, J.F. Wang, X.D. Zhang, Z.Y. Jiang, *Journal of Physics D: Applied Physics*, 2013, **46**, 105306.
- 47 K. Palanisamy, J.H. Um, M. Jeong, W.S. Yoon, *Scientific Reports*, 2016, **6** (July), 1–12.
- 48 L.Y. Beaulieu, T.D. Hatchard, A. Bonakdarpour, M.D. Fleischauer, J.R. Dahn, *Journal of Electrochemical Society*, 2003, **150** (11), A1457–A1464.
- 49 J. Sakabe, N. Ohta, T. Ohnishi, K. Mitsuishi, K. Takada, *Communications Chemistry*, 2018, **1** (24), 1–9.
- 50 D. Uxa, B. Jerliu, E. Huger, L. Dorrer, M. Horisberger, J. Stahn, H. Schmidt, *Journal of Physical Chemistry C*, 2019, **123**, 22027–22039.
- 51 Y.S. Yoon, S.H. Lee, S.B. Cho, S.C. Nam, *Journal of The Electrochemical Society*, 2011, **158** (12), A1313.
- 52 L. Baggetto, D. Mohanty, R.A. Meisner, C.A. Bridges, C. Daniel, D.L. Wood, N.J. Dudney, G.M. Veith, *RSC Advances*, 2014, **4** (45), 23364–23371.
- 53 B.J. Hwang, C.Y. Wang, M.Y. Cheng, R. Santhanam, *Journal of Physical Chemistry C*, 2009, **113** (26), 11373–11380.
- 54 K.F. Chiu, *Thin Solid Films*, 2007, **515** (11), 4614–4618.
- 55 J. Mürter, S. Nowak, E. Hadjixenophontos, Y. Joshi, G. Schmitz, *Nano Energy*, 2018, **43**, 340–350.
- 56 Y. Zhang, L.Z. Ouyang, C.Y. Chung, M. Zhu, *Journal of Alloys and Compounds*, 2009, **480** (2), 981–986.